Fuel 341 (2023) 127403

Contents lists available at ScienceDirect

Fuel

journal homepage: www.elsevier.com/locate/fuel

Full Length Article

Ammonia-methane combustion in a swirl burner: Experimental analysis and numerical modeling with Flamelet Generated Manifold model

Dániel Füzesi [a,*], Siqi Wang [b], Viktor Józsa [a], Cheng Tung Chong [b]

[a] Department of Energy Engineering, Faculty of Mechanical Engineering, Budapest University of Technology and Economics, Műegyetem rkp. 3, H-1111 Budapest, Hungary

[b] China-UK Low Carbon College, Shanghai Jiao Tong University, Lingang, Shanghai 201306, China

ARTICLE INFO

Keywords:
Combustion
CFD
Ammonia
Burner
Swirl
PIV

ABSTRACT

Ammonia/methane flames gained significant attention since this is a probable step toward a sustainable, carbon-free economy in the near future. Therefore, three such flames were numerically and experimentally investigated in a swirl burner, focusing on robust modeling methods to facilitate the spreading of ammonia combustion in the industry. Chemistry was considered by the mechanism of Okafor and employed through the Flamelet Generated Manifold model. Both Particle Image Velocimetry and OH* measurements confirmed the appropriateness of the numerical model in all cases. It was demonstrated that the modeling approaches are applicable at both near stoichiometric conditions and close to the flammability limit of ammonia. The comparison of steady-state and the mean unsteady results implied that the steady calculations are appropriate only for the chemical conversion and fall behind in flow field modeling. The Root Mean Square velocity was identical up to the reaction zone for all cases, while its value decreased with the increase of ammonia concentration. The CO emission matched underpredicted experiments by a magnitude; however, the concentration was very low. Regarding the NO_x emission, the CFD underpredicted it by a factor of two.

1. Introduction

Ammonia is an excellent energy carrier since it is carbon-free, sulfur-free, and significantly easier to handle than either liquefied or pressurized hydrogen while having a higher calorific value per both mass and volume than that [1]. Consequently, NH_3 is a highly prospective alternative fuel [2]. A critical advantage of NH_3 over H_2 is the easier long-term storage and lower susceptibility to leakages due to its larger molecular size [3]. The presence of nitrogen in the fuel is problematic from a NO_x emission point of view, which can be mitigated by CH_4 [4] or H_2 dilution [5] through the extension of the flammability range of pure NH_3, which is equivalence ratio, ϕ, of 0.7–1.3 under atmospheric conditions [6]. The present paper aims to robustly model CH_4/NH_3 combustion in a swirl burner, which is widely used in utility boilers, industrial furnaces, and gas turbines [7]. The numerical results were validated by Particle Image Velocimetry, PIV, and OH* chemiluminescence measurements.

Enabling robust calculations in computational fluid dynamics, CFD, software greatly facilitates the spreading NH_3 utilization in the industry. Sun et al. [8] analyzed a swirl burner fueled by NH_3/H_2 mixtures with a Reynolds-Averaged Navier Stokes, RANS, simulation, using the re-Normalization Group, RNG, k-ε viscosity model. Combustion was modeled by the Eddy Dissipation Concept, EDC, using a simplified model of Okafor et al. [9] by eliminating the hydrocarbon reactions, ending up with 19 species and 63 reactions. To reduce the computational demand, swirl vanes were considered only through the boundary conditions. Even though the match in hydrodynamics is good, chemistry needs advanced approaches, as highlighted in [10]. Wei et al. [11] performed a Large Eddy Simulation, LES, on a swirl burner, including the swirler, using the mechanism of Xiao et al. [12] with 31 species and 243 reactions. Chemistry was considered via a dynamic thickened flame model in the OpenFOAM software environment. The validation by PIV and OH-Planar Laser-Induced Fluorescence showed an excellent agreement. The mesh size was about five million cells, and solving the problem needed 120,000 processor hours per case [13]. A further critical advantage of this model is the capability of fairly simulating the lean blowout behavior of the flame [14]. The combination of LES with flamelet-generated manifold, FGM, also provides excellent agreement with experiments [15]. The critical advantage of the FGM method is that the chemistry is simplified into two variables: the mean mixture fraction

* Corresponding author.
E-mail address: fuzesi.daniel@gpk.bme.hu (D. Füzesi).

https://doi.org/10.1016/j.fuel.2023.127403
Received 28 July 2022; Received in revised form 24 December 2022; Accepted 2 January 2023

and the progress variable, resulting in a massive reduction of the computational demand. This is the reason why this approach was selected for the present study.

The use of LES and a few million cells do not ultimately lead to appropriate numerical results. Franco et al. [16] investigated an NH_3/H_2 flame both experimentally and numerically, using a flamelet model and the mechanism of Glarborg et al. [17]. The comparison of numerical and experimental results was not explicitly presented, while there is more than a 300 °C temperature difference between them in the intense reaction zone, projecting discrepancies in heat release rate modeling. The temperature measurement was burdened with 8 % uncertainty using a PtRh-Pt thermocouple.

The advantage of the NH_3/CH_4 fuel mixture is that the two reaction pathways are weakly connected [18]. Mikulčič et al. [19] modeled NH_3/CH_4-air combustion in the AVL Fire software environment. Their final mesh size was 155,436 cells, which enables computationally cheap simulations using the mechanisms of Okafor et al. [9] (42 species, 130 reactions), Konnov et al. [20] (51 species, 420 reactions), and the San Diego group [21] (68 species and 330 reactions). The viscous model was the k-ϵ, and chemistry was considered via the General Gas Phase Reactions model. The swirler was modeled via the boundary conditions, and the geometry of [22] was used. The validation was performed via concentrations of various species in the flue gas with a reasonable agreement in NO under rich conditions, while that of lean combustion was overestimated by a factor of two. Overall, the three mechanisms behaved similarly for O_2, CO_2, and CO. M. O. V. Zuniga et al. [23] used the Okafor mechanism [9] in a swirl combustor to simulate ammonia/hydrogen blends by RANS with periodicity, which could bias the numerical results for the 3D flow structures, typical in swirl burners. Otherwise, the results were validated only with emission measurement, where the model overpredicted the NO emission. At the same time, the flow field agreed with the PIV data only in one case under cold conditions.

Ammonia contains a single nitrogen atom in each molecule, meaning the inevitable presence of fuel-bonded nitrogen. Consequently, NO and NO_2 form more easily during oxidation than from the atmospheric N_2, which is especially critical in gas turbines [24]. Another nitrogen oxide is N_2O, which has 273 times higher global warming potential, GWP, than CO_2 over 100 years [25]. Therefore, N_2O emissions will also be critically evaluated. If the combustion temperature is sufficiently high, N_2O will be converted to NO [26], which is not listed as a gas with global warming potential. However, its adverse effect on human health and the environment should be taken seriously.

The novelty of this paper is the numerical analysis of CH_4/NH_3 flame near the lean flammability limit of NH_3, using FGM for reaction modeling in CFD. A further non-trivial part of the numerical analysis is comparing and evaluating unsteady and steady simulations since this simplification cannot generally be made for swirl burners. The numerical results were validated by PIV and OH* measurements. Then the chemical conversion along the axis is presented, focusing on the transient characteristics. Finally, the measured and simulated pollutant emissions were compared.

2. Materials and methods

This section is divided into two parts. The first one presents the experimental setup, including the burner, the test conditions, flame imaging, and the PIV and OH* measurements. Secondly, the numerical setup is detailed, focusing on the governing equations, the models, the mesh, and the boundary conditions.

2.1. Experimental setup

2.1.1. Swirl flame burner

An atmospheric swirl flame burner is used to establish the ammonia-methane premixed flames. The burner is made of stainless steel, while the combustor wall is a square-shaped quartz chamber of 80 × 80 × 200 mm, as shown in Fig. 1. The quartz chamber allows optical access for flame visualization and non-intrusive laser diagnostics. An axial swirler is located at the burner outlet concentric to the combustor wall. The swirler comprises eight straight guide vanes of 1.5 mm in thickness located at 45° from the centerline axis. The inner and outer diameters of the annular channel containing the swirl vanes were 21 and 38.6 mm, respectively. The swirling intensity of the flow is estimated via the geometric swirl number equation of

$$S_N = \frac{2}{3}\left[\frac{1-(D_h/D_s)^3}{1-(D_h/D_s)^2}\right]\tan\theta, \quad (1)$$

where D_h and D_s are the diameter of the swirler hub and swirler, respectively, while θ is the angle between the swirler vane and centerline axis. The geometric swirl number was 0.77, which is sufficiently strong to produce a high swirl intensity flow ($S_N > 0.6$). Fig. 1 shows the schematic of the swirl flame burner and the flow delivery system. The air and fuel flows are regulated by the mass flow controllers [Sevenstar series: air and methane (model CS230) and ammonia (model CS200)] with an accuracy of ±1.0 % of the full scale. Due to the corrosive nature of ammonia, a PTFE tube was used to deliver ammonia to the burner plenum for mixing with air and methane. The well-premixed fuel/air exits the burner outlet through the swirler to be combusted and stabilized by the bluff body of the swirler hub at atmospheric conditions. The ammonia and methane used to have a purity of 99.999 % and 99.99 %, respectively. The fuels were mixed before the burner inlet, and fuel and air streams were introduced to the center of a cylinder with an 80 mm inner diameter and 56 mm height. The cylinder upstream of the swirler was 42 mm in inner diameter and 343 mm in length.

2.1.2. Operating conditions

The premixed ammonia/methane/air flames were established under swirling conditions based on the operating conditions, as shown in Table 1. Three cases of varied NH_3 and CH_4 blend compositions were selected as test cases, denoted as Cases A, B, and C. The main swirling air flow supplied to the burner was kept constant for all three cases at 2.568 g/s to provide similar cold flow conditions in all cases. Case A and B are supplied with different fuel blend compositions, consisting of 20 % NH_3 and 80 % CH_4 by volume, while the latter is comprised of 50 % NH_3 and 50 % CH_4. The different heating values of fuels result in different thermal power and global fuel–air equivalence ratio, ϕ_{global}. Case B has a similar ϕ_{global} and power output as case C, but the blend ratio of the fuels is different. Case B requires a higher mass flow of ammonia to level the flame thermal output than case C. Case A has a higher flame thermal output than case C despite the same fuel blend ratio, as the former has higher overall fuel input, which leads to a higher ϕ_{global} and thermal power output. All the cases are established at fuel-lean conditions to simulate the typical flames used in gas turbine combustors.

2.1.3. Flame structure imaging

The actual flame images were captured using a digital camera (SONY SLT-A35) with a resolution of 3568 × 2368 pixels. The camera was set with an aperture of f/2 and an exposure time of 1/25 s. To examine the heat release zone of the flames, an intensified CCD camera (LaVision, Imager SX 4M) coupled with a bandpass filter (Thorlabs, 308 nm ± 5 nm) was utilized to capture the excited OH* chemiluminescence from the flames. The CCD camera has a resolution of 2360 × 1776 pixels, while the image intensifier (LaVision, IRO X) was set with a gain of 90 %, 9×10^5 ns gate, and delay of 200 ns to amplify the signals. 150 image pairs were taken for each flame condition to obtain the average flame signals at 15 Hz repetition rate. The 2D average line-of-sight images were deconvoluted via Abel transformation to obtain the representative centerline planar flame structure.

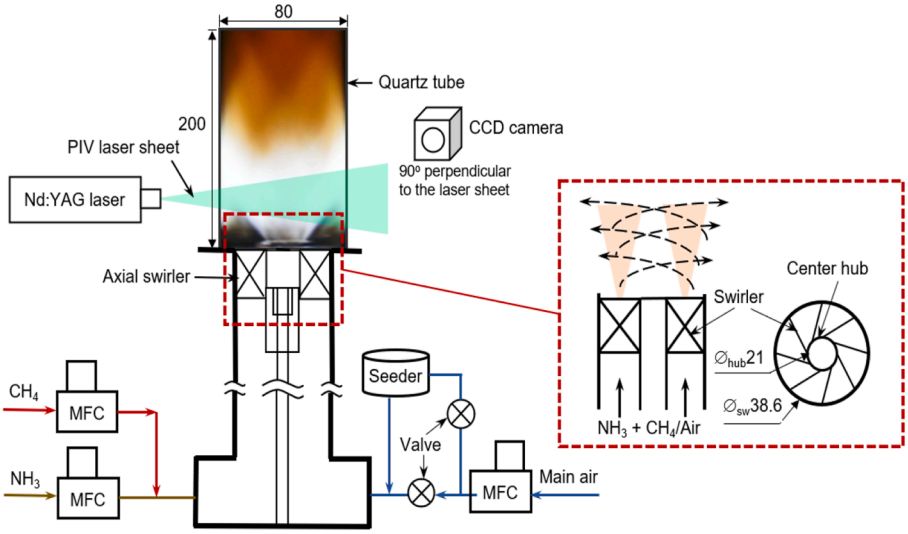

Fig. 1. Swirl burner and flow delivery system. All dimensions are in mm.

Table 1
Operating conditions of the premixed swirl flames of binary fuel blends.

Case	NH_3:CH_4 (v/v %)	$\dot{m}_{air}$ (g/s)	$\dot{m}_{NH_3}$ (g/s)	$\dot{m}_{CH_4}$ (g/s)	ϕ_{global}	Power (kW)
A	20:80	2.586	0.034	0.128	0.93	7.04
B	50:50	2.586	0.085	0.08	0.73	5.59
C	20:80	2.586	0.027	0.103	0.74	5.63

2.1.4. Reacting flow field measurement

The flow field within the swirl flame burner is investigated via a 2D low-speed PIV system (LaVision Flow Master 2D). The PIV system consists of a dual-head, double-pulse Nd:YAG laser (Litron) and a CCD camera (LaVision Imager SX). The laser pulse energy used was ~50 mJ/pulse, generating a light sheet of 0.5 mm at 532 nm to illuminate the seeding particles (TiO_2 with a mean diameter of 1 μm). The primary swirl air was split into two parts to enable the seeding of fine particles into the mixture. A fraction of air (~17 %) was bypassed to the solid particle generator (LaVision, Particle Blaster 110) to generate seeding for mixing with the bulk air and fuel at the burner plenum. The planar laser sheets reflect the signal from the particles captured by the CCD camera that is placed perpendicularly, as shown in Fig. 1. The lens of the camera (Nikkor lens 60 mm/F2.8) was installed with an optical band-pass filter centered at 532 nm to prevent saturation due to the strong flame luminosity. The acquired images were processed using the cross-correlation algorithm in the LaVision Davis software with an interrogation window of 48 × 48 pixels with a 50 % overlap for the initial pass, followed by 32 × 32 pixels with a 50 % overlap for the cross-correlation procedure. The accuracy of the axial and radial velocity measurement is determined to be ±1.25 % full scale, based on the ratio of the nominal correlation peak value (0.1 pixels) to the maximum displacement permitted, which is 1/4 of the final interrogation window (32 × 32 pixels) [27].

2.1.5. Post-combustion emissions measurement

Measurement of the exhaust emissions of the flames was conducted via a gas analyzer (KANE 9206 Quintox) at the combustor outlet. The combustion tube has a length of 350 mm to allow for homogenous mixing of the post-combustion gases. The pollutant emissions of CO, NO, and NO_2 are sampled using a tube with a diameter of 5 mm at the sampling rate of 2 L/min. The uncertainties of the measured values for the present operating conditions are ±5 ppm for CO and NO_2 and ±5 % for NO.

2.2. Theory and modeling

2.2.1. Governing equations of turbulent flow

This sub-subsection summarizes the governing equations of turbulent, compressible flow without considering reacting flow since the combustion model is detailed in Sub-subsection 2.2.2. The mass, momentum, and energy conservations are described in Eqs. (2), (3), and (4), respectively. The derivation of these equations for reacting gas mixture can be found, e.g., in Ref. [28]. The conservation of mass by continuity equation according to Eq. (2):

$$\frac{\partial \rho}{\partial t} + \nabla(\rho \underline{u}) = 0, \tag{2}$$

where ρ is the density of the fluid, and $\underline{u} = \underline{u}(u, v, w)^T$ is the continuous phase velocity of the gas mixture. Momentum conservation is considered through the Navier-Stokes equations:

$$\frac{\partial(\rho \underline{u})}{\partial t} + \nabla(\rho \underline{u}\,\underline{u}) = \rho \underline{g} - \nabla p + \nabla \boldsymbol{\tau}, \tag{3}$$

where p is the static pressure, $\boldsymbol{\tau}$ is the stress tensor, and g is the gravitational acceleration here. The energy equation in terms of the specific enthalpy:

$$\frac{\partial(\rho h)}{\partial t} + \nabla(\rho \underline{u} h) - \nabla\left(\frac{\lambda}{c_p}\nabla h\right) = \nabla \underline{J_h}, \tag{4}$$

where λ is the thermal conductivity of the gas, h is the specific enthalpy, c_p is the specific heat capacity at constant pressure, $\underline{J_h}$ is the diffusion flux of enthalpy, and t is time. Furthermore, the ideal gas model was considered for the compressible flow:

$$\rho = \frac{p_{op} + p}{\frac{R}{\bar{M}} T}, \tag{5}$$

where R is the universal gas constant, p_{op} is the operating (ambient) pressure, p is the overpressure, and $\bar{M}$ is the average molar mass of the

mixture, which is calculated as:

$$\frac{1}{\bar{M}} = \sum_{i=1}^{N} \frac{Y_i}{M_i}, \tag{6}$$

where Y_i and M_i are the mass fractions and molar mass of the ith species for N species.

2.2.2. Flamelet generated manifold (FGM)

The combustion model was partially premixed with the C Equation [29], where the laminar flame speed is calculated from the 1D reaction mechanism through flamelets. Chemistry was considered by the non-adiabatic FGM model [10], which is equivalent to the 2D-FGM [15]. The FGM model assumes that the multi-dimensional turbulent flame is an ensemble of 1D laminar flamelets [30]. The built-in flamelet generator of the ANSYS Fluent software was used to create laminar flamelets in the physical space, which uses the premixed flamelet generator of ANSYS Chemkin-Pro. The governing equations are detailed in Sub-subsection 2.2.1., which are supplemented with the balance equation of mass for the mixture species in Eq. (7).

$$\frac{\partial(\rho Y_i)}{\partial t} + \nabla(\rho \underline{u} Y_i) + \nabla\cdot\left(\rho \underline{V_i} Y_i\right) = \omega_i, \; i = 1, 2\cdots N-1, \tag{7}$$

where $\underline{V_i}$, is the velocity, and ω_i is the reaction rate. Note that Eq. (7) is solved for N-1 species since $\sum_{i=1}^{N} Y_i = 1$. The equations of the reacting flow can be reformulated to the flamelet equations; more details can be found in [30]. The laminar flamelets are solved at different enthalpy levels to consider the heat loss via the combustion chamber walls during the FGM tabulation process. Hence the specific enthalpy should be considered as follows:

$$h_i = h_{i,ref} + \int_{T_{ref}}^{T} c_{p,i}(T')\mathrm{d}T', \tag{8}$$

where $h_{i,ref}$ is the enthalpy of formation at the reference temperature, which was 298.15 K during the flamelet calculations, representing the laboratory ambient temperature. $c_{p,i}$ is the specific heat capacity of the species i. During the flamelet generation, each flamelet was solved at 21 enthalpy values at 32 mixture fraction levels. To retrieve the thermo-chemical variables during the 3D CFD calculation, the reaction progress variable (γ) is used as a control variable besides the enthalpy, which should be defined as the linear combinations of species mass fraction as a monotonic function:

$$\gamma = \sum_{i=1}^{N} \alpha_i Y_i, \tag{9}$$

where α_i coefficients are the weight factors, which are chosen arbitrarily to provide monotonicity for γ. In this study, $\alpha_i = 0$ for all species except $\alpha_{CO_2} = \alpha_{CO} = 1$. An automated grid refinement was used for the reaction progress generation, which is built-in into the software, creating 102 points. The FGM is included in the CFD code by solving transport equations for the control variables. For the progress variable:

$$\frac{\partial(\rho\gamma)}{\partial t} + \nabla\cdot(\rho\underline{u}\gamma) - \nabla\cdot\left(\frac{\lambda}{c_p}\nabla\gamma\right) = \nabla\cdot\left[\frac{\lambda}{c_p}\sum_{i=1}^{N}\alpha_i\left(\frac{1}{\mathrm{Le_i}} - 1\right)\nabla Y_i\right] + \omega_\gamma, \tag{10}$$

where $\mathrm{Le_i}$ is the Lewis numbers of the considered species, and ω_γ is the progress variable source term defined by $\omega_\gamma = \sum_{i=1}^{N}\alpha_i\omega_i$. Similarly, the transport equation for the enthalpy:

$$\frac{\partial(\rho h)}{\partial t} + \nabla\cdot(\rho\underline{u}h) - \nabla\cdot\left(\frac{\lambda}{c_p}\nabla h\right) = \nabla\cdot(D_h\nabla\gamma), \tag{11}$$

where D_h is the preferential diffusion coefficient. For generating non-adiabatic 1D flamelets, the reduced mechanism of Okafor [9] was used with 42 species and 130 reaction steps. Since the partially-premixed model was applied, the mixture fraction was considered an additional control variable. The variances of the control variables were also solved. As the Okafor mechanism includes NO and NO_2 reactions, no separate NO_x formation model was needed. The mixture ignition was performed by patching the entire domain with a progress variable value of one.

2.2.3. Thermal radiation modeling

The discrete ordinates model, DO, was used to consider thermal radiation. DO solves the radiative transfer equation, which can be written in the form of Eq. (12) in the $\vec{s}$ direction [31]:

$$\nabla(I(\vec{r},\vec{s})\vec{s}) + (\alpha+\sigma_s)I(\vec{r},\vec{s}) = \frac{\alpha n^2\sigma T^4}{\pi} + \frac{\sigma_s}{4\pi}\int_0^{4\pi} I(\vec{r},\vec{s}')\phi(\vec{s}\cdot\vec{s}')\mathrm{d}\Omega', \tag{12}$$

where, $I(\vec{r},\vec{s})$ is the radiation intensity depending on the $\vec{r}$ position and $\vec{s}$ direction. α is the absorption coefficient of the medium, σ_s is the scattering coefficient, s is the path length, n is the refractive index of the medium, σ is the Stefan-Boltzmann constant, T is the local temperature, ϕ is the phase function, Ω' is the solid angle, and $\vec{s}$ is the discrete direction which is associated with discrete solid angles. The model assumes a finite number of discrete angles that should be discretized. The octants of the angular space are discretized into the polar (θ) and the azimuthal (ϕ) control angles. Hence, their divisions determine the number of control angles, which was considered 2. The scattering coefficient was not considered in our model, while for α the weighted-sum-of-grey-gases model was used. Furthermore, the refractive index of the medium was assumed to be unity.

2.2.4. Numerical setup and procedure

The numerical problem was entirely solved in ANSYS Fluent 2021 R1. Hence the mesh was created in its mesh tool following the instructions of [32], using the geometry of the burner, shown schematically in Fig. 1. According to the mesh sensitivity analysis, the final mesh size was 374,051 cells, considering the temperature, velocity, pressure, and concentration distributions through various control lines passing high gradients. The final mesh is shown in Fig. 2.

Both steady-state and transient simulations were performed and compared, detailed in Subsection 3.2. The convective Courant number was confined below 0.65 in the entire combustion chamber. The time step size of 10 μs with 10 inner iterations was applied, and a total time of 0.1 s was simulated to have a developed flow. The unsteady calculations were preceded by steady-state ones, providing the initial conditions. Reynolds Averaged Navier-Stokes, RANS, simulations were carried out for the steady-state case with the k-ω SST turbulence model, while the unsteady RANS Scale Adaptive Simulation turbulence model was used during the transient simulations.

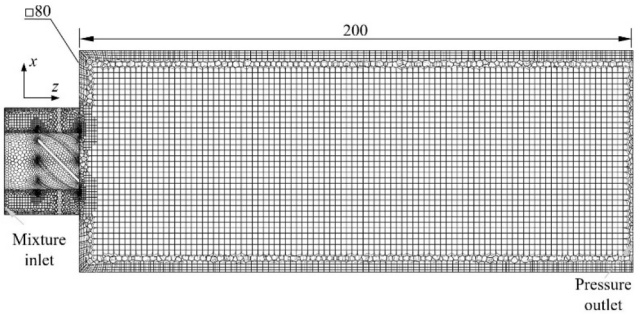

Fig. 2. Volumetric mesh of the swirl burner and the combustion chamber.

Table 2
Boundary conditions.

BC type	Value
Flue gas pressure outlet gauge pressure [Pa]	0
Operating pressure [Pa]	101,325
Heat transfer coefficient for the mixing tube wall [W/m^2 K] [33]	9.7
Heat transfer coefficient for the combustion chamber wall [W/m^2 K] [33]	13.44
Ambient temperature [°C]	25
Emissivity for steel tube [–] [34]	0.5
Emissivity for fused silica combustion chamber [–] [35]	0.75
Other walls	adiabatic

Regarding the material properties, the ideal gas law was applied for the density, while temperature-dependent thermal conductivity and dynamic viscosity of air were used for the mixture. Furthermore, temperature-dependent specific heat was estimated via a simple mixing law rule. The boundary conditions are presented in Table 2, while the mass flow rates of the investigated cases were adopted from Table 1. The wall thermal boundary conditions were treated as mixed-type, so both the convection and radiation were considered; furthermore, the thermal conductivity of the walls was also considered.

The pressure-based solver was used with a second-order interpolation scheme with the SIMPLE pressure interpolation algorithm for velocity–pressure coupling, while a bounded central differencing scheme was applied for the momentum equation and a bounded second-order implicit scheme for temporal discretization. For the rest of the equations, second-order schemes were used, summarized in Table 3.

3. Results and discussion

Firstly, this section begins validating the numerical model via flame images, OH* images, and PIV measurements. Subsection 3.2 compares the steady-state and time-averaged results to evaluate the appropriateness of generally used steady simulations. Note that the presented numerical results outside this subsection originated from unsteady calculations unless stated otherwise. Thirdly, characteristic species are evaluated through the combustion chamber axis, while Subsection 3.4 focuses on the flow field. Finally, pollutant formation was compared with measurement data in Subsection 3.5.

3.1. Validation

Flame images and simulated temperature distribution of all three cases are shown in Fig. 3, highlighting the V-shaped flame, characteristic of swirling combustion. The least luminous flame was observed in Case B. The luminosity in Case C was higher due to the increased CH_4 share in the mixture, which has increased flame speed [6] and features strong CH emission at 431 nm [36], making the flame bluer. The most luminous flame was observed in Case A, where the same fuel mixture was used as in Case C, while the thermal power was increased. Therefore, the intense reaction zone is the longest in Case B due to the lower reactivity of the NH_3, which is discussed next.

Table 3
Spatial discretization schemes.

Scalar equation	Discretization scheme
Density	
Turbulent kinetic energy	
Specific dissipation rate	
Energy	
Discrete ordinates	Second-order upwind
Progress variable	
Mean mixture fraction	
Progress variable variance	
Mixture fraction variance	

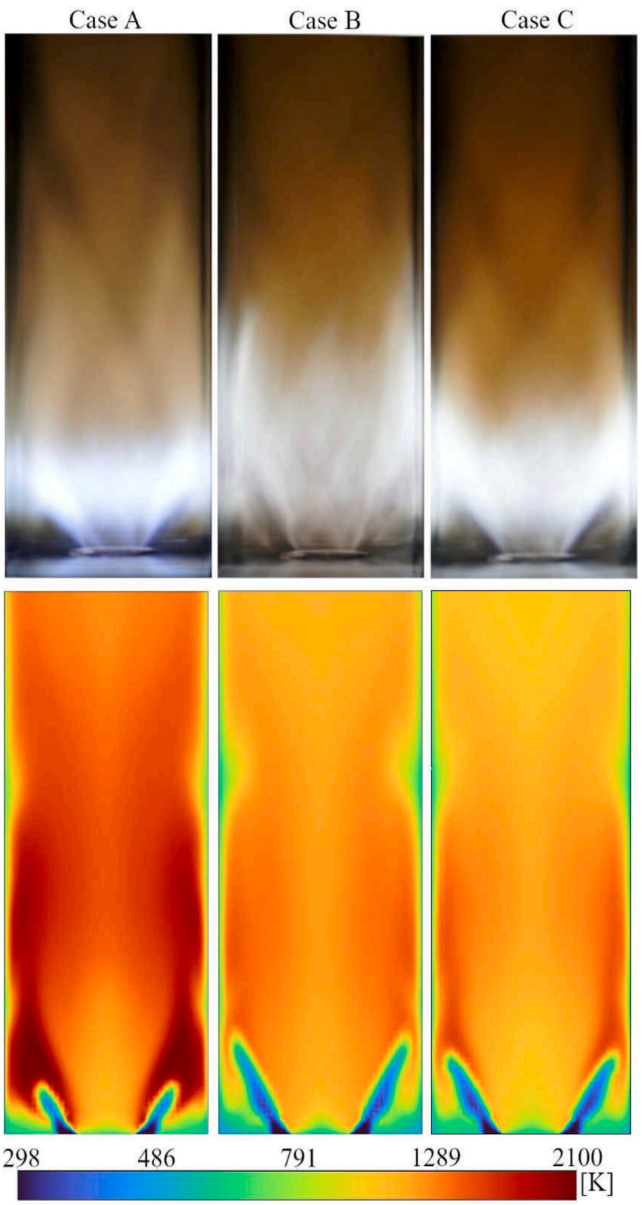

Fig. 3. Flame image (top) and mean temperature distribution (bottom).

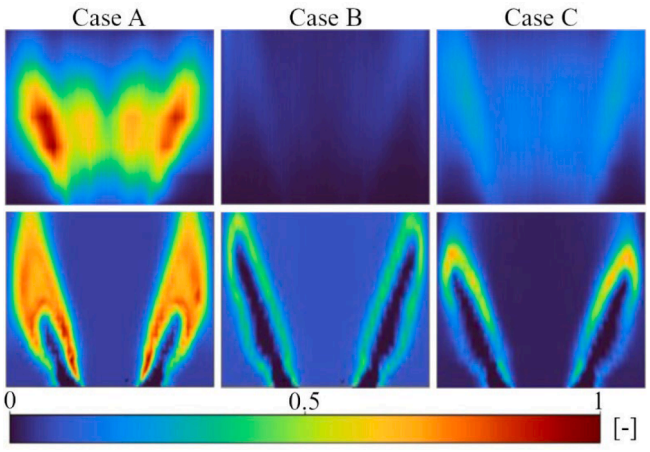

Fig. 4. Measured OH* intensity after Abel transformation (top) and mean OH mass fraction distribution by CFD (bottom).

Fig. 4 shows the measured OH* and simulated OH mass fraction distribution in an 80 × 40 mm^2 window at the bottom of the combustion chamber. Note that the system is only capable of measuring the excited OH, OH*, which is mostly generated via the following two routes [37]:

$$CH + O_2 \rightarrow CO + OH^*, \quad (R1)$$

$$H + O + M \rightarrow OH^* + M. \quad (R2)$$

Reaction (1) has a higher probability if the CH_4 concentration is higher, while (R2) is independent of the fuel type, but it is a trimolecular reaction with a lower probability under atmospheric conditions. This answers the significant intensity difference between Case B and the others. The difference between Case A and C is the equivalence ratio; the lower intensity was observed at lower ϕ_{global}. Case A also featured higher thermal power due to the increased fuel flow rate. Since the Okafor mechanism did not contain OH*, the OH distribution was compared with the measurement data with qualitatively consistent results to the measurement data. The difference originated from the fact that (R1) is a more likely reaction if the CH_4 share is increased. Otherwise, the OH* and OH distributions are similar. The intense heat release is present in a larger volume in Case A, while the peaks of Cases B and C are located closer to the walls at the tip of the stems of V.

The vector field of each case is presented in Fig. 5, up to 80 mm in the combustion chamber, comparing the results of the PIV measurements and CFD. The inner and outer recirculation zones can be found at the same position for the measurements and CFD results in each case. The same characteristics and magnitudes were observed in [14] by PIV and LES.

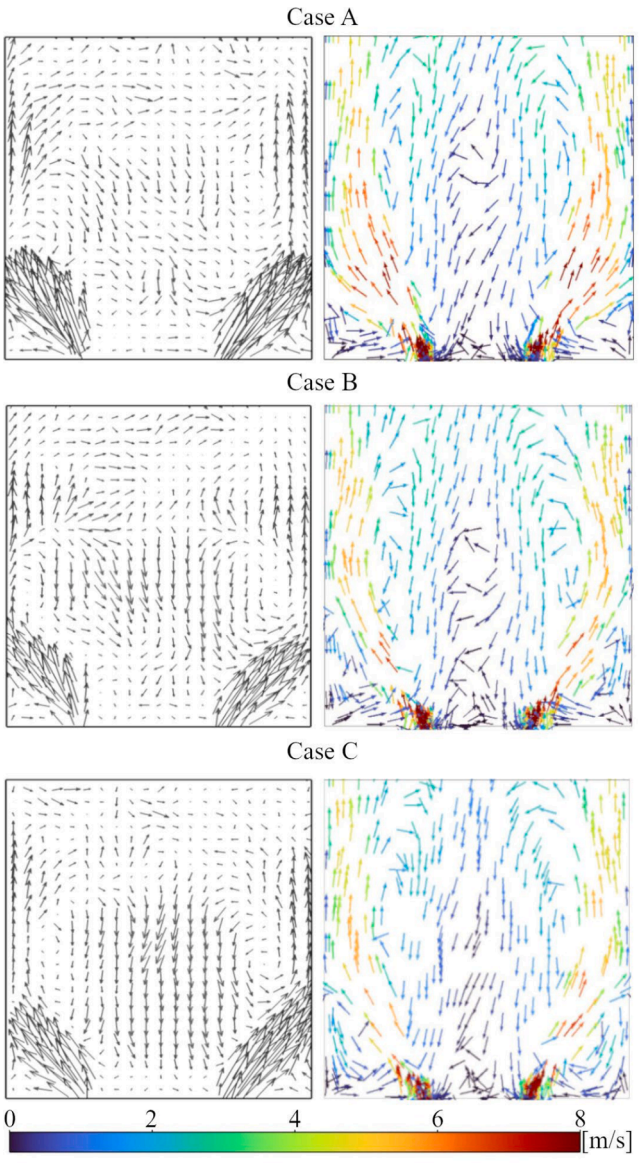

Fig. 5. Measured (top) and calculated mean 2D velocity vector field CFD (bottom).

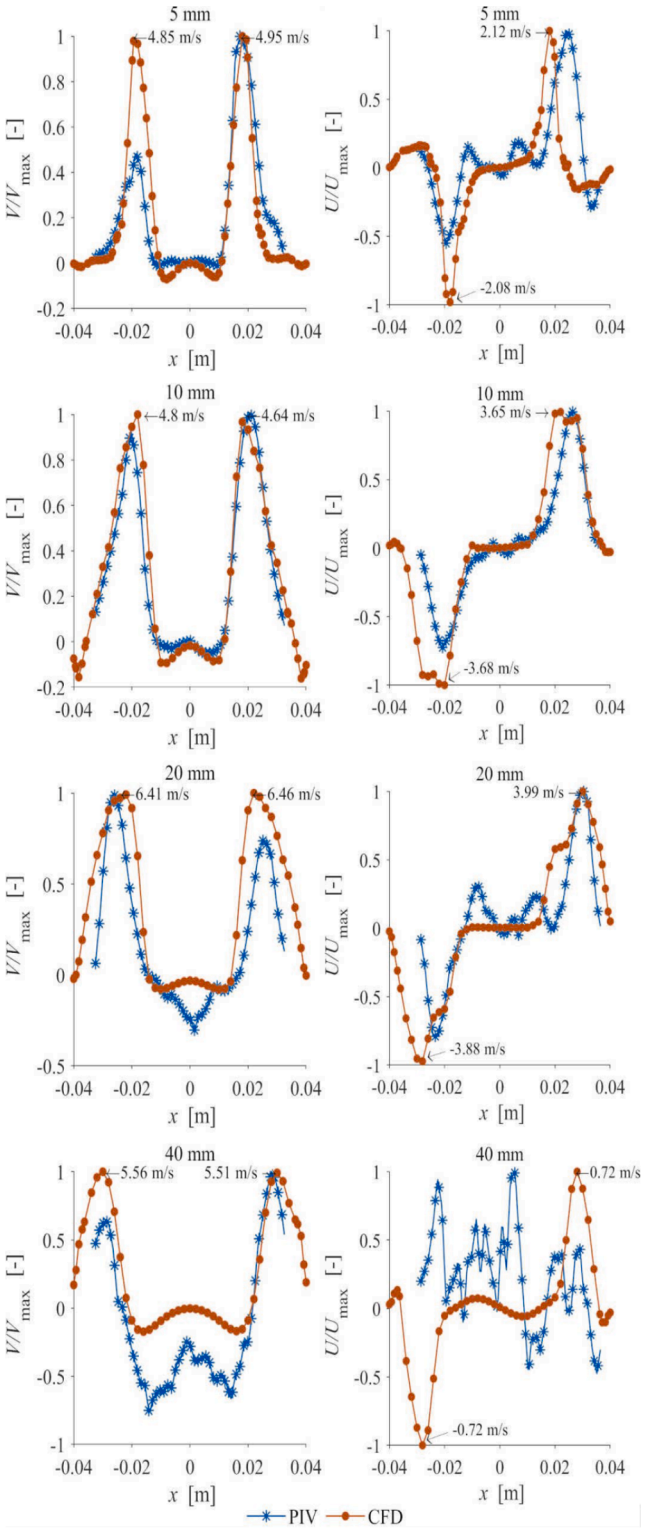

Fig. 6. Axial (left) and radial (right) velocity components along the *x*-axis at different heights for Case A. Note the maximum values in each plot.

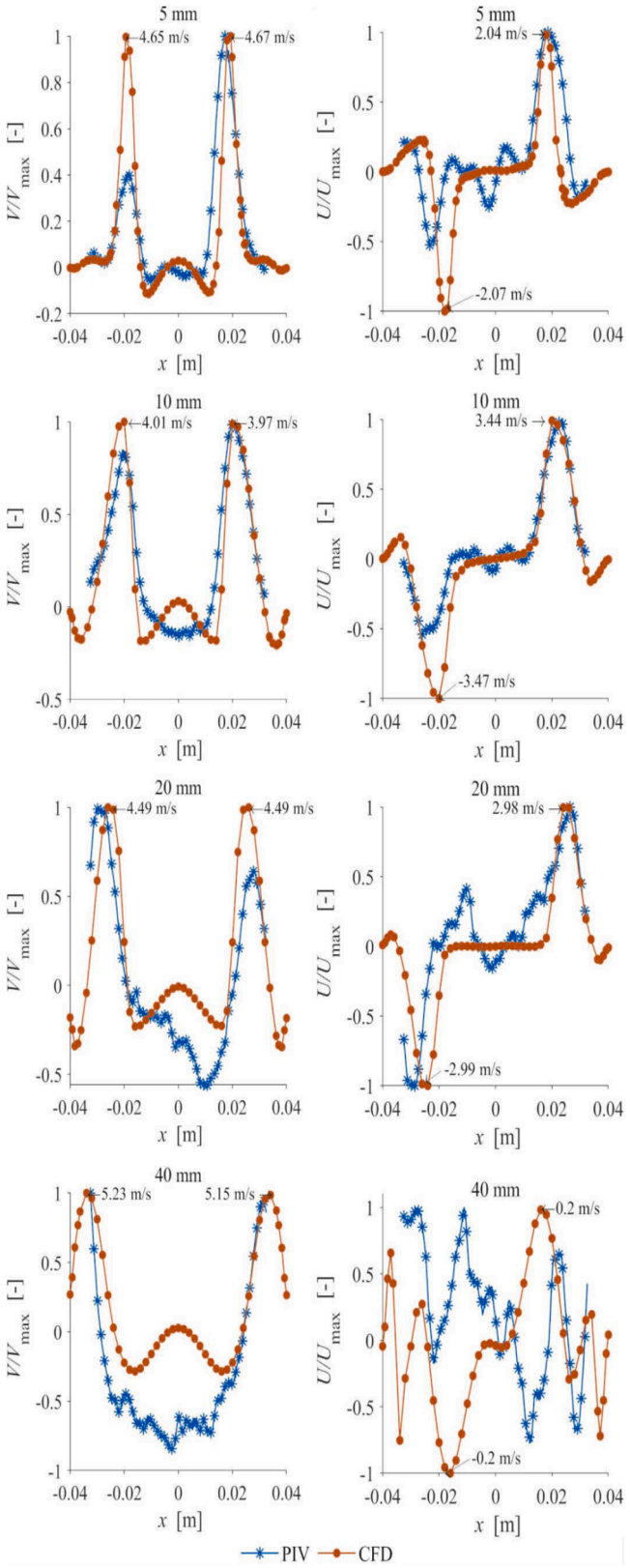

Fig. 7. Axial (left) and radial (right) velocity components along the *x*-axis at different heights for Case B. Note the maximum values in each plot.

The quantitative validation of the axial and radial velocity components can be seen in Figs. 6–8 for each case at different heights from the burner tip up to 40 mm along the *x*-axis. At all heights, the data were divided by the maxima, a common practice for CFD-PIV comparison

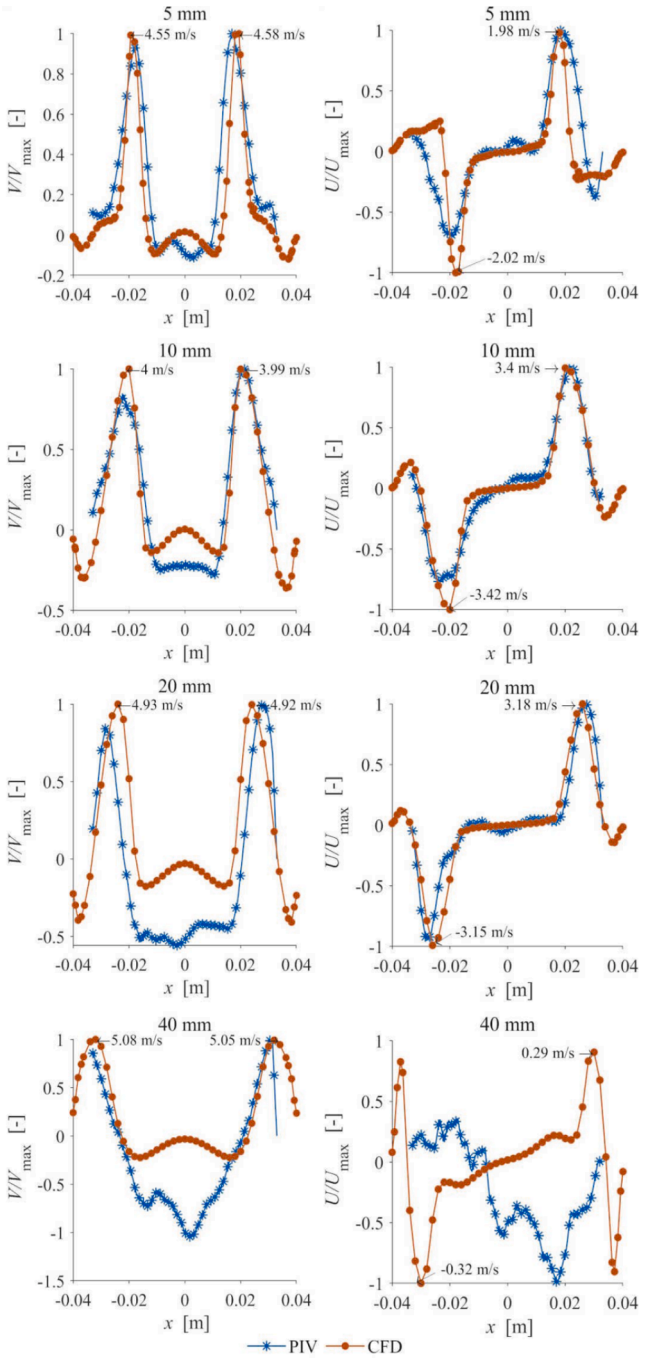

Fig. 8. Axial (left) and radial (right) velocity components along the *x*-axis at different heights for Case C. Note the maximum values in each plot.

[38,39]. The CFD results are symmetric, while the measurements show an asymmetric profile, probably caused by the imperfect geometry and uneven seeder particle distribution. After 20 mm, the values at the inner recirculation zone are smaller in the case of PIV, caused by the lower particle density. This phenomenon can be recognized in the case of the radial component as well, where most velocity values are smaller than 1 m/s, comparable to the uncertainty of the technique. Otherwise, the match is acceptable for all cases.

3.2. *Steady vs. unsteady results*

Turbulent combustion simulation generally requires transient formulation [10], while some researchers prefer steady-state

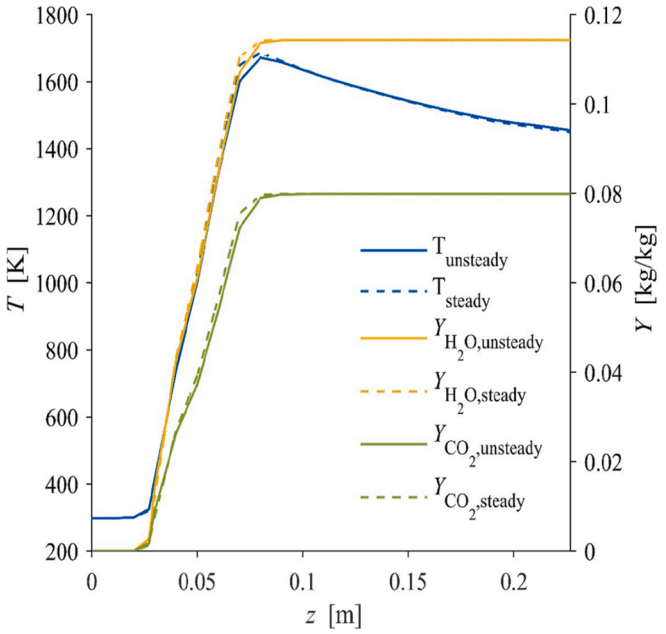

Fig. 9. Steady-state and mean unsteady products and temperature profile along the combustion chamber axis.

calculations without verifications [40,41]. The inevitable advantage of this simplification is that a relatively high number of cells can be used with detailed chemistry at a low computational cost. However, proper control is mandatory. Therefore, this section compares the steady-state and the mean unsteady results of Case B.

Fig. 9 shows CO_2 and H_2O concentrations and the temperature profile in the combustion chamber. The results imply that the unsteady time-averaged and the steady cases match. Furthermore, the pollutants also match the outlet detailed in Table 4. Although the surface-averaged values perfectly agree, the radial distributions show slight differences, as shown in Fig. 10. The velocity peaks nearly match; however, the inner recirculation zone is underestimated near the tip of the mixing tube while overestimated towards the outlet. The distribution matches the temperature profile, while the values are higher in the inner zone and decay to the same values after 150 mm. In conclusion, the average values on the axial surfaces will not differ in the steady-state simulation cases, meaning that this simplification is helpful in calculating average profiles and general chemical conversion. However, if the reaction zone and the flow field are of primary importance, unsteady calculations are essential.

3.3. Reaction zone characteristics

Fig. 11 shows the integrated mass-weighted averages on axial surfaces with the Root Mean Square, RMS, values of the temperature. The earliest ignition occurs in Case A, followed by Case C. The difference can be explained by the lower equivalence ratio in Case C, while the higher thermal power causes the larger temperature peak. The slower heat release in Case B is due to the lower reactivity of NH_3 compared to CH_4. The intense reaction zone is confined to the positive temperature

Table 4
Steady and unsteady averaged emission at the outlet in ppm at 15 % O_2 in the dry flue gas.

Cases	Steady-state	Transient
CO	7.787	7.797
NO	2260	2260
NO_2	3.351	3.351

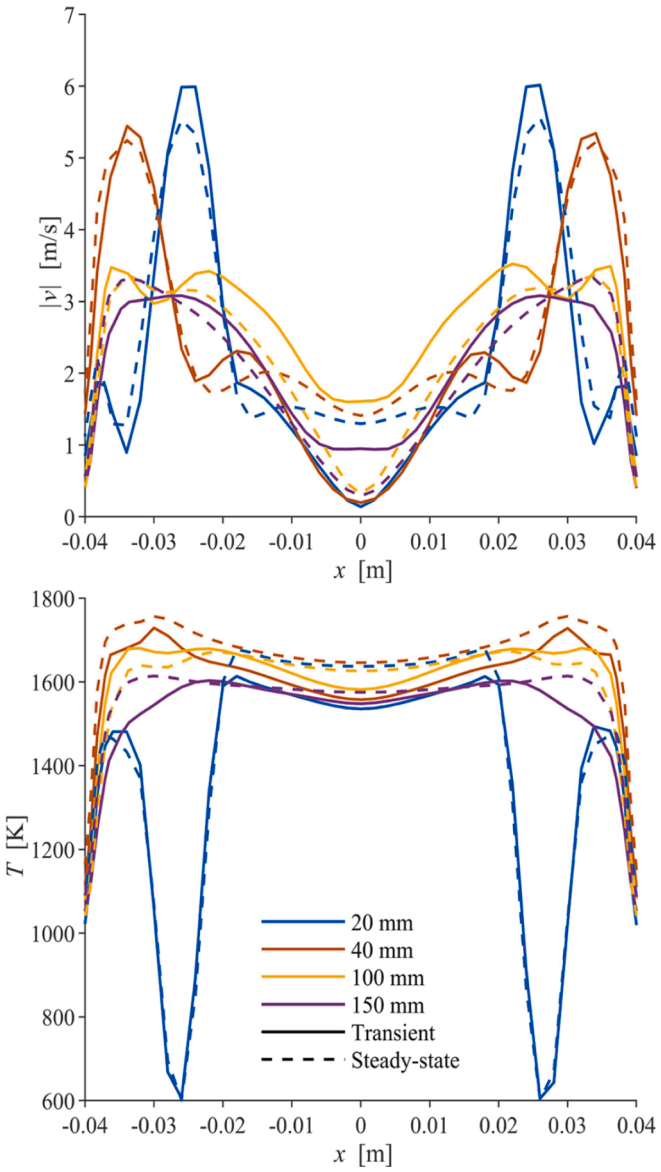

Fig. 10. Steady and mean unsteady velocity and temperature profiles along the *x*-axis at various downstream distances.

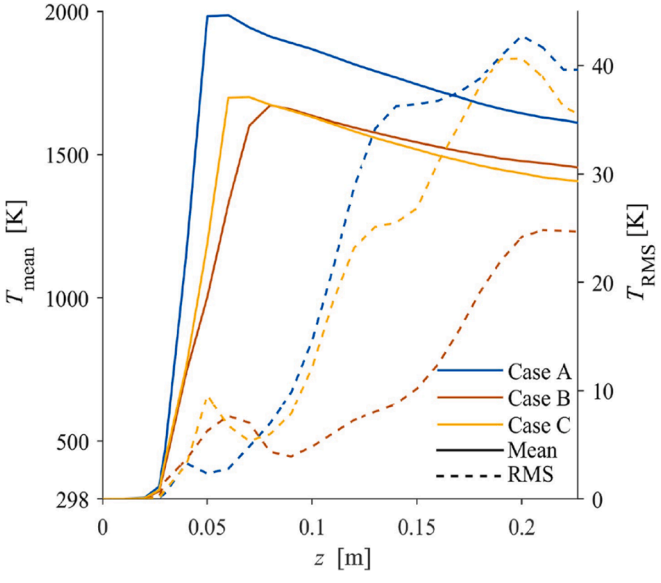

Fig. 11. Mean and RMS temperature profiles along the combustion chamber.

gradient zone, while most heat is released by the temperature peak [42]. After this point, the temperature decreases due to heat loss. The RMS values also start to increase from this point due to the vortex structures and the inhomogeneous heat release on planes perpendicular to the flow direction, as shown in Subsection 3.4. The RMS values along the combustion chamber similarly increase in all cases, while that of Case B is smaller due to the longer reaction zone. Measured from the temperature peak, all trends match.

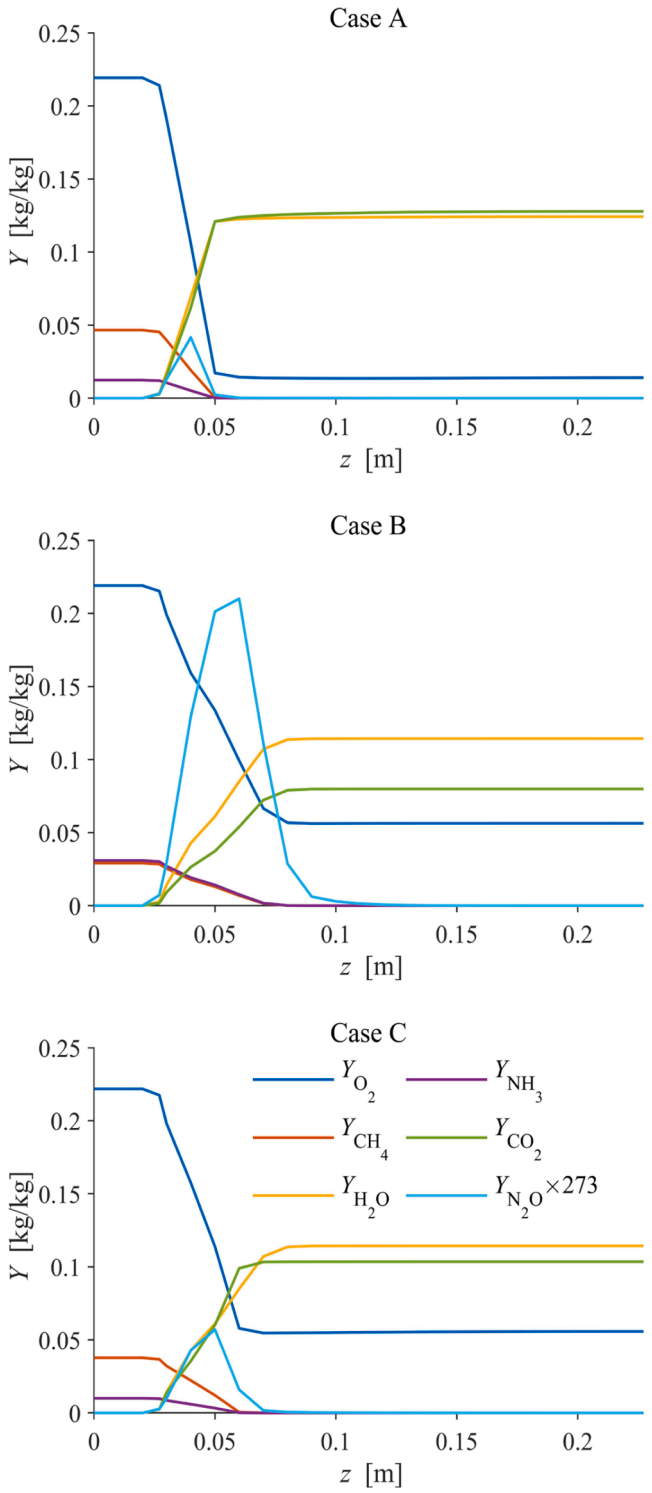

Fig. 12. Mean profile of O_2, NH_3, CH_4, CO_2, H_2O, and N_2O in the combustion chamber. Note that the legend is shared.

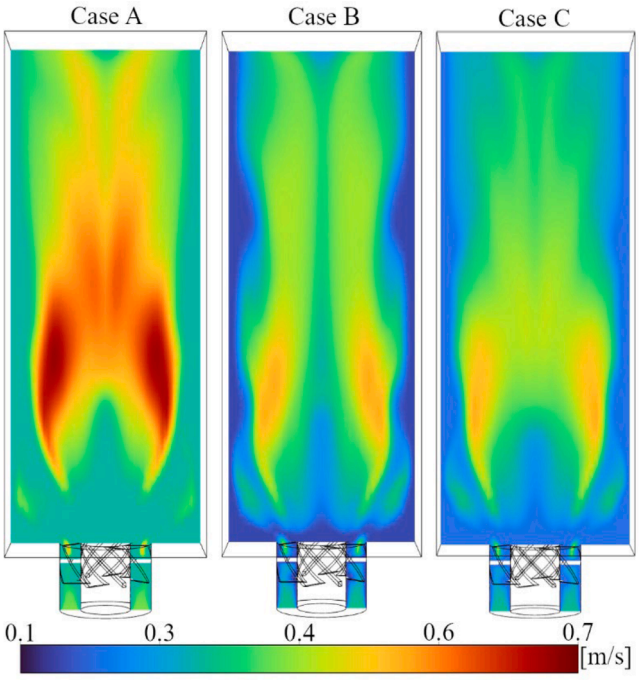

Fig. 13. Mean turbulent flame speed distribution.

The consumption of the reactants and the formation of final products can be seen in Fig. 12. The N_2O was added and multiplied by its GWP. It was only present in the reaction zone as an intermediate product and consumed by the end of the flame. The N_2O concentration was the highest in Case B due to the higher NH_3 concentration, which increased with the equivalence ratio. The appearance of CO_2 and H_2O is located at $z = 25$ mm in all cases. The shortest intense reaction zone is 25 mm long in Case A due to the combined effect of increased thermal power and higher ϕ.

The turbulent flame speed is presented in Fig. 13. Cases A and C are qualitatively similar, and the different thermal power causes the quantitative difference. Despite the different fuel compositions, the maximum turbulent flame speed is the same in Cases B and C. The non-

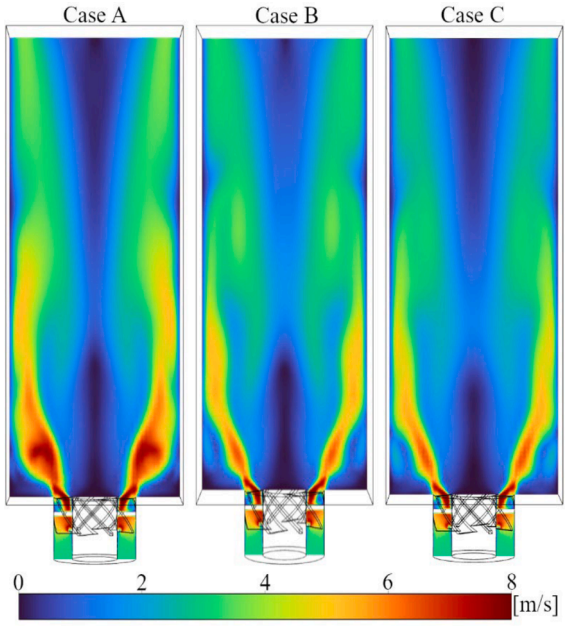

Fig. 14. Mean velocity magnitude distribution.

zero turbulent flame speed towards the outlet shows that the reactions continue in the combustion chamber regardless that the majority of the heat release occurred up to 0.1 m, and there is no significant variation in the concentration of the most important species, as shown in Figs. 11 and 12. Therefore, non-zero flame speed does not imply an intense reaction zone; slower reactions with small species concentrations can occur due to the high temperature. The higher flame speed values are confined to the bottom region since the main heat release occurs here, where the heat release is the most intense. The higher CH_4 concentration increases the turbulent flame speed in line with [3].

3.4. Flow field

The turbulent cold flow is greatly affected by the spatial and temporal characteristics of the chemical reactions. The mean velocity magnitude contains the typical inner and outer recirculation zones [43], as shown in Fig. 14. Case A shows higher velocities due to the higher thermal power, while Cases B and C match regardless of the different fuel compositions. The surface integral values along the combustion chamber are shown in Fig. 15, including the RMS values. Since the combustion air flow rate was identical for all cases, and the fuel flow rate was inferior up to the reaction zone, detailed in Fig. 12, the velocity trends are the same. The RMS values of Cases A and C are similar, especially downstream of the reaction zone, concluding that the fuel composition governs the velocity fluctuations. The 50 % NH_3 content results in halved RMS velocity values.

3.5. Pollutant emission

Pollutant emissions significantly affect our environment and can also be used for validation. However, it enables only the comparison with measurement data at the outlet or within the flame, but the probe is an invasive sensor in this latter case. The former allows only the evaluation of the flue gas without providing information on the reactions. Since the validation of the flame structure was performed via PIV and OH* measurements, the CO, NO, and NO_2 concentrations were compared only at the outlet. According to the European gas turbine emission standard [44], the results are recalculated to a dry flue gas at a 15 % O_2 level.

Fig. 16 presents the CO distribution in the combustion chamber. The highest value occurs in Case A, which burns out by the outlet. Thermal power is marginal here; the higher concentration in Case A results from

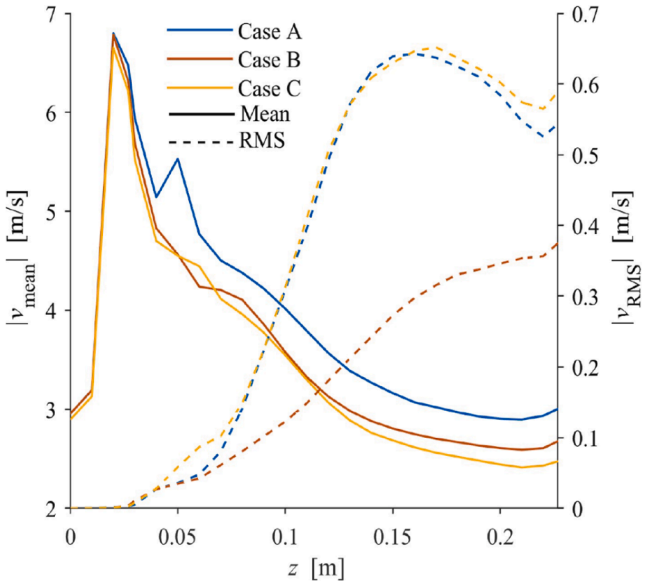

Fig. 15. Mean and RMS velocity profile in the combustion chamber.

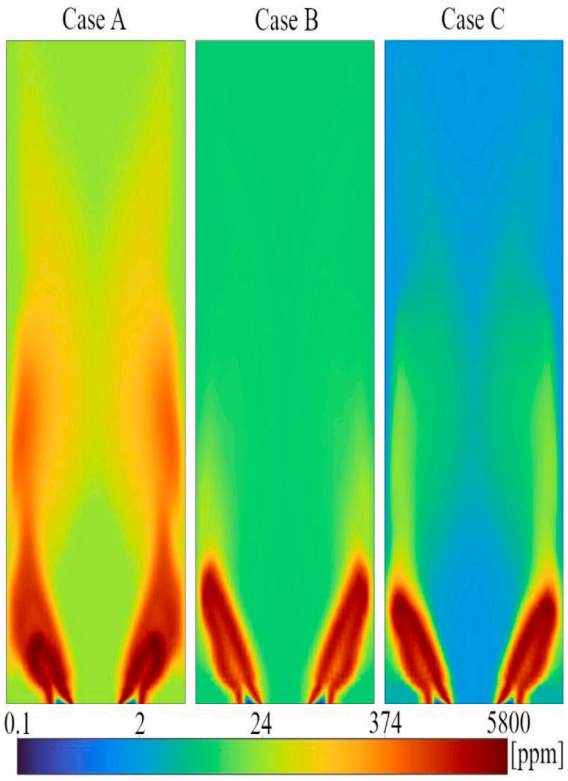

Fig. 16. Mean CO distribution at 15% O_2 in the dry flue gas. Note the log scale.

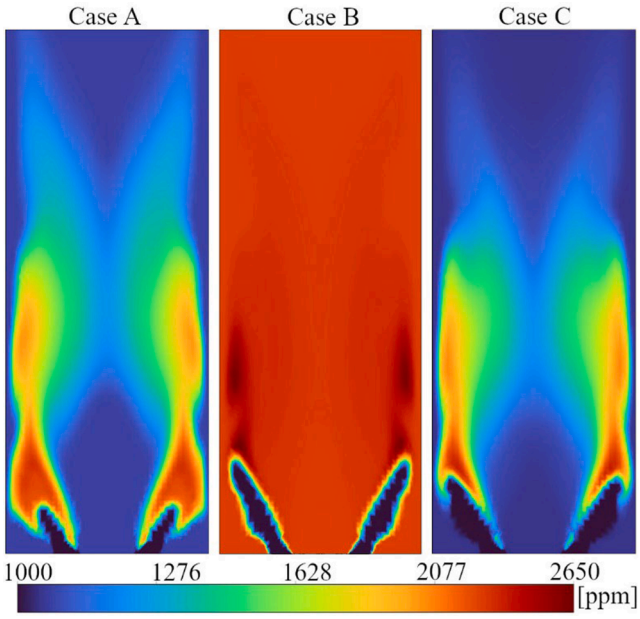

Fig. 17. Mean NO distribution at 15% O_2 in the dry flue gas. Note the log scale.

the higher ϕ_{global}. Therefore, the V shape of Cases B and C is similar. Since the CO emission at the outlet is in the range of 10 ppm, practically complete combustion is present in all cases.

The NO and NO_2 production were presented in Figs. 17 and 18, concluding that NO_2 formation is marginal; most nitrogen oxides are NO. The 1000 ppm range does not comply with standards [44], presenting the challenge of environmentally friendly NH_3 combustion. NO emission does not scale linearly with the NH_3 concentration in the fuel; even small NH_3 shares lead to excessive emission levels in the currently

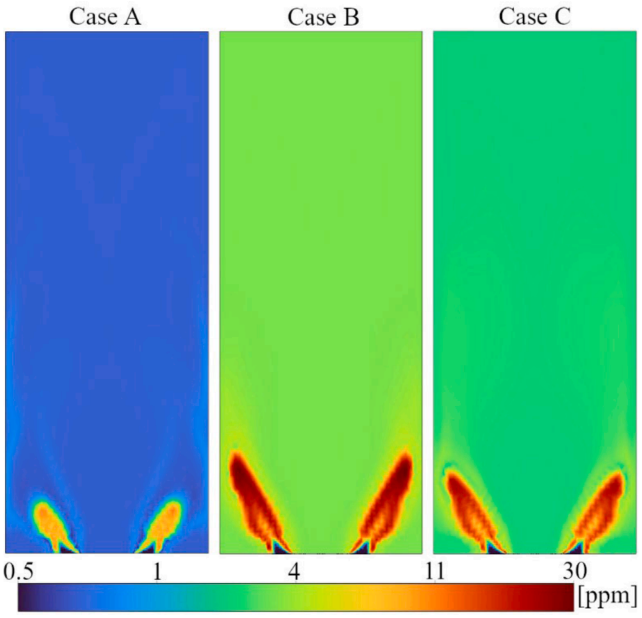

Fig. 18. Mean NO_2 distribution at 15% O_2 in the dry flue gas. Note the log scale.

Table 5
Simulated CO and NO_x emission in ppm at 15 % O_2 in the dry flue gas.

Cases	A	B	C	C_{meas}
CO	23.4	7.8	1.45	11.5
NO_x	1072.4	2263.6	1051.7	2178

used burners. Obviously, the NO concentration increases with NH_3 share.

The emission measurement was performed in a different combustion chamber geometry with a 120 × 120 mm^2 base and 350 mm length. This variant was made of steel instead of glass. The calculations were performed in the steady state, following the results of Subsection 3.2, i.e., steady simulations are sufficient for checking the conversion globally. The mass-weighted average CFD results are shown in Table 5. CO was low in all cases, and the 80 % CH_4 features halved total NO_x production. NH_3 of 2.5 % in CH_4 leads to 1300 ppm emission [40], showing that the NO emission is a general problem in NH_3 co-combustion, and its clean combustion is marginally affected by its concentration in the fuel. The flue gas measurements were performed only in Case C. The CO emission was missed by one magnitude; however, the absolute values are very low compared to the Hungarian standard in force for new gas turbine plants [45]. This pollutant is absent in the related European standard [44]. The NO_x formation was underpredicted by a factor of two, unlike in [19,23]. The difference is probably caused by the richer conditions in the cited references. Also, in [46], where the numerical results of a two-element chemical reactor network model underpredicted the emission with similar order of magnitude, while overpredictions occurred with higher order models. Consequently, more work is needed on the NH_3 mechanisms that recently gained outstanding attention.

4. Conclusions

The combustion of three ammonia/methane blends was investigated by numerical simulations focusing on robust modeling of the reaction zone, the flow field, and the emissions. The main findings are the following:

1. Using FGM with the mechanism of Okafor provided a good match with a relatively small mesh for all three NH_3/CH_4 blends in a turbulent swirl burner, validated PIV, OH*, and emission measurements. Since Case B and C were investigated near the lean flammability limit of NH_3, the robustness of the model was presented.
2. The steady-state and mean unsteady results were compared, concluding that steady approaches are usable only for characterizing the global chemical conversion. Otherwise, simulations benefit more from the transient formulation than they lose in simpler chemistry.
3. The RMS of the temperature and the velocity magnitude along the axis showed that significant fluctuations occur after the reaction zone, while it is negligible before ignition.
4. The NO_x, CO, and N_2O were evaluated along the combustion and at the outlet. The N_2O was practically converted to NO by the outlet, while CO was low in each case compared to current pollutant emission regulations. NO_x doubled with the increase of NH_3 from 20 % to 50 %.

Funding

The research reported in this paper was supported by the National Research, Development and Innovation Fund of Hungary, project N°. OTKA-FK 137758, and TKP2021 Grant N°. BME-NVA-02, ÚNKP-22-5-BME-304, and ÚNKP-22-3-II-BME-100 New National Excellence Program by the Ministry for Culture and Innovation of Hungary from the National Research, Development and Innovation Fund, and the János Bolyai Research Scholarship of the Hungarian Academy of Sciences (Hungarian researchers). The funding support from Shanghai Jiao Tong University (Grant No. WF220428004) for the experimental work is gratefully acknowledged.

CRediT authorship contribution statement

Dániel Füzesi: Conceptualization, Methodology, Validation, Investigation, Formal analysis, Writing – original draft, Writing – review & editing, Visualization, Software, Data curation. **Siqi Wang:** Validation, Investigation, Writing – original draft, Writing – review & editing, Visualization, Data curation. **Viktor Józsa:** Conceptualization, Methodology, Validation, Investigation, Formal analysis, Resources, Writing – original draft, Writing – review & editing, Visualization, Supervision, Project administration, Funding acquisition. **Cheng Tung Chong:** Validation, Investigation, Writing – original draft, Writing – review & editing, Resources, Funding acquisition, Supervision.

Declaration of Competing Interest

The authors declare the following financial interests/personal relationships which may be considered as potential competing interests: Daniel Fuzesi reports financial support was provided by Ministry for Culture and Innovation of Hungary. Viktor Jozsa reports financial support was provided by Ministry for Culture and Innovation of Hungary. Viktor Jozsa reports financial support was provided by Hungarian Academy of Sciences.

Data availability

Data will be made available on request.

References

[1] Kobayashi H, Hayakawa A, Somarathne KDKA, Okafor EC. Science and technology of ammonia combustion. Proc Combust Inst 2019;37:109–33. https://doi.org/10.1016/j.proci.2018.09.029.

[2] Chai WS, Bao Y, Jin P, Tang G, Zhou L. A review on ammonia, ammonia-hydrogen and ammonia-methane fuels. Renew Sustain Energy Rev 2021;147:111254. https://doi.org/10.1016/j.rser.2021.111254.

[3] Valera-Medina A, Amer-Hatem F, Azad AK, Dedoussi IC, de Joannon M, Fernandes RX, et al. Review on Ammonia as a Potential Fuel: From Synthesis to Economics. Energy Fuels 2021;35:6964–7029. https://doi.org/10.1021/acs.energyfuels.0c03685.

[4] Ariemma GB, Sorrentino G, Ragucci R, de Joannon M, Sabia P. Ammonia/Methane combustion: Stability and NOx emissions. Combust Flame 2022;241:112071. https://doi.org/10.1016/j.combustflame.2022.112071.

[5] Khateeb AA, Guiberti TF, Wang G, Boyette WR, Younes M, Jamal A, et al. Stability limits and NO emissions of premixed swirl ammonia-air flames enriched with hydrogen or methane at elevated pressures. Int J Hydrogen Energy 2021;46:11969–81. https://doi.org/10.1016/j.ijhydene.2021.01.036.

[6] Glassman I, Yetter R. Combustion. 4th ed. Burlington: Academic Press; 2008.

[7] Lefebvre AH, Ballal DR. Gas turbine combustion. 3rd ed. Boca Raton: CRC Press; 2010. doi:10.1002/1521-3773.

[8] Sun Y, Cai T, Shahsavari M, Sun D, Sun X, Zhao D, et al. RANS simulations on combustion and emission characteristics of a premixed NH3/H2 swirling flame with reduced chemical kinetic modeltable 1. Chin J Aeronaut 2021. https://doi.org/10.1016/j.cja.2020.11.017.

[9] Okafor EC, Naito Y, Colson S, Ichikawa A, Kudo T, Hayakawa A, et al. Measurement and modelling of the laminar burning velocity of methane-ammonia-air flames at high pressures using a reduced reaction mechanism. Combust Flame 2019;204:162–75. https://doi.org/10.1016/j.combustflame.2019.03.008.

[10] Poinsot T, Veynante D. Theoretical and Numerical Combustion. 3rd ed. Bordeaux: T. Poinsot; 2012.

[11] Wei X, Zhang M, An Z, Wang J, Huang Z, Tan H. Large eddy simulation on flame topologies and the blow-off characteristics of ammonia/air flame in a model gas turbine combustor. Fuel 2021;298:120846. https://doi.org/10.1016/j.fuel.2021.120846.

[12] Xiao H, Howard M, Valera-Medina A, Dooley S, Bowen PJ. Study on Reduced Chemical Mechanisms of Ammonia/Methane Combustion under Gas Turbine Conditions. Energy Fuel 2016;30:8701–10. https://doi.org/10.1021/acs.energyfuels.6b01556.

[13] Zhang M, An Z, Wang L, Wei X, Jianayihan B, Wang J, et al. The regulation effect of methane and hydrogen on the emission characteristics of ammonia/air combustion in a model combustor. Int J Hydrogen Energy 2021;46:21013–25. https://doi.org/10.1016/j.ijhydene.2021.03.210.

[14] Zhang M, Wei X, Wang J, Huang Z, Tan H. The blow-off and transient characteristics of co-firing ammonia/methane fuels in a swirl combustor. Proc Combust Inst 2021;38:5181–90. https://doi.org/10.1016/j.proci.2020.08.056.

[15] An Z, Zhang M, Zhang W, Mao R, Wei X, Wang J, et al. Emission prediction and analysis on CH4/NH3/air swirl flames with LES-FGM method. Fuel 2021;304:121370. https://doi.org/10.1016/j.fuel.2021.121370.

[16] Franco MC, Rocha RC, Costa M, Yehia M. Characteristics of NH3/H2/air flames in a combustor fired by a swirl and bluff-body stabilized burner. Proc Combust Inst 2021;38:5129–38. https://doi.org/10.1016/j.proci.2020.06.141.

[17] Mei B, Zhang X, Ma S, Cui M, Guo H, Cao Z, et al. Experimental and kinetic modeling investigation on the laminar flame propagation of ammonia under oxygen enrichment and elevated pressure conditions. Combust Flame 2019;210:236–46. https://doi.org/10.1016/j.combustflame.2019.08.033.

[18] Okafor EC, Naito Y, Colson S, Ichikawa A, Kudo T, Hayakawa A, et al. Experimental and numerical study of the laminar burning velocity of CH4–NH3–air premixed flames. Combust Flame 2018;187:185–98. https://doi.org/10.1016/j.combustflame.2017.09.002.

[19] Mikulčić H, Baleta J, Wang X, Wang J, Qi F, Wang F. Numerical simulation of ammonia/methane/air combustion using reduced chemical kinetics models. Int J Hydrogen Energy 2021;46:23548–63. https://doi.org/10.1016/j.ijhydene.2021.01.109.

[20] Li R, Konnov AA, He G, Qin F, Zhang D. Chemical mechanism development and reduction for combustion of NH3/H2/CH4 mixtures. Fuel 2019;257:116059. https://doi.org/10.1016/j.fuel.2019.116059.

[21] Jiang Y, Gruber A, Seshadri K, Williams F. An updated short chemical-kinetic nitrogen mechanism for carbon-free combustion applications. Int J Energy Res 2020;44:795–810. https://doi.org/10.1002/er.4891.

[22] Valera-Medina A, Marsh R, Runyon J, Pugh D, Beasley P, Hughes T, et al. Ammonia–methane combustion in tangential swirl burners for gas turbine power generation. Appl Energy 2017;185:1362–71. https://doi.org/10.1016/j.apenergy.2016.02.073.

[23] Vigueras-Zuniga MO, Tejeda-Del-Cueto ME, Vasquez-Santacruz JA, Herrera-May AL, Valera-Medina A. Numerical predictions of a swirl combustor using complex chemistry fueled with ammonia/hydrogen blends. Energies 2020;13. https://doi.org/10.3390/en13020288.

[24] Cerinski D, Vujanović M, Petranović Z, Baleta J, Samec N, Hriberšek M. Numerical analysis of fuel injection configuration on nitrogen oxides formation in a jet engine combustion chamber. Energy Convers Manag 2020;220:112862. https://doi.org/10.1016/j.enconman.2020.112862.

[25] Intergovernmental Panel on Climate Change. Climate Change 2022: Mitigation of Climate Change 2022.

[26] Mohammadpour A, Mazaheri K, Alipoor A. Reaction zone characteristics, thermal performance and NOx/N2O emissions analyses of ammonia MILD combustion. Int J Hydrogen Energy 2022;47:21013–31. https://doi.org/10.1016/j.ijhydene.2022.04.190.

[27] Wernet MP. Development of digital particle imaging velocimetry for use in turbomachinery. Exp Fluids 2000;28:97–115. https://doi.org/10.1007/s003480050015.

[28] Williams F. Combustion Theory. Redwood City: Addison-Wesley Publishing Company; 1985.

[29] Zhang K, Ghobadian A, Nouri JM. Comparative study of non-premixed and partially-premixed combustion simulations in a realistic Tay model combustor. Appl Therm Eng 2017;110:910–20. https://doi.org/10.1016/j.applthermaleng.2016.08.223.

[30] van Oijen JA, Donini A, Bastiaans RJM, ten Thije Boonkkamp JHM, de Goey LPH. State-of-the-art in premixed combustion modeling using flamelet generated manifolds. Prog Energy Combust Sci 2016;57:30–74. https://doi.org/10.1016/j.pecs.2016.07.001.

[31] Inc. ANSYS. Ansys Fluent Theory Guide. Release 2021R1. Canonsburg: 2021.

[32] ANSYS Inc. 5 Best Practices for Gas Turbine Combustion Meshing Using Ansys Fluent. Canonsburg: 2020.

[33] Martin M, Holge K, editors. VDI Heat Atlas. 2nd ed. Berlin, Heidelberg: Springer-Verlag Berlin Heidelberg; 2010.

[34] Technologies L. Table of emissivity of various surfaces. Schaffhausen: Mikron Instrument Company, Inc.; 2003.

[35] Barnes BT, Forsythe WE, Adams EQ. The total emissivity of various materials at 100–500 degrees C. J Opt Soc Am 1947;37:804–7. https://doi.org/10.1364/JOSA.37.000804.

[36] Gaydon AG. The spectroscopy of flames. 2nd ed. Chapman and Hall Ltd., London; 1974. doi:10.1016/0010-2180(75)90098-X.

[37] Panoutsos C, Hardalupas Y, Taylor A. Numerical evaluation of equivalence ratio measurement using OH* and CH* chemiluminescence in premixed and non-premixed methane–air flames. Combust Flame 2009;156:273–91. https://doi.org/10.1016/j.combustflame.2008.11.008.

[38] Sun Y, Cai T, Shahsavari M, Sun D, Sun X, Zhao D, et al. RANS simulations on combustion and emission characteristics of a premixed NH3/H2 swirling flame with reduced chemical kinetic model. Chin J Aeronaut 2021;34:17–27. https://doi.org/10.1016/j.cja.2020.11.017.

[39] Taamallah S, Dagan Y, Chakroun N, Shanbhogue SJ, Vogiatzaki K, Ghoniem AF. Helical vortex core dynamics and flame interaction in turbulent premixed swirl combustion: A combined experimental and large eddy simulation investigation Helical vortex core dynamics and flame interaction in turbulent premixed swirl combustion: A combi. Phys Fluids 2019;31:025108. https://doi.org/10.1063/1.5065508.

[40] Jójka J, Ślefarski R. Emission Characteristics for Swirl Methane-Air Premixed Flames with Ammonia Addition. Energies 2021;14:662. https://doi.org/10.3390/en14030662.

[41] Sun J, Yang Q, Zhao N, Chen M, Zheng H. Numerically study of CH4/NH3 combustion characteristics in an industrial gas turbine combustor based on a reduced mechanism. Fuel 2022;327:124897. https://doi.org/10.1016/j.fuel.2022.124897.

[42] Law CK. Combustion Physics. New Jersey: Cambridge University Press; 2010.

[43] Somarathne KDKA, Colson S, Hayakawa A, Kobayashi H. Modelling of ammonia/air non-premixed turbulent swirling flames in a gas turbine-like combustor at various pressures. Combust Theory Model 2018;22:973–97. https://doi.org/10.1080/13647830.2018.1468035.

[44] European Parliament. Directive (EU) 2015/2193 of the European Parliament and of the Council of 25 November 2015 on the limitation of emissions of certain pollutants into the air from medium combustion plants. Off J Eur Union 2015;313.

[45] Ministry of Agriculture. Decree 53/2017 for the pollutant emissions of combustion systems with greater than 140 kWth and less than 50 kWth thermal power 2017.

[46] Zhang M, An Z, Wei X, Wang J, Huang Z, Tan H. Emission analysis of the CH4/NH3/air co-firing fuels in a model combustor. Fuel 2021;291:120135. https://doi.org/10.1016/j.fuel.2021.120135.